RSC Advances

PAPER

View Article Online
View Journal | View Issue

Cite this: *RSC Adv.*, 2026, **16**, 10538

Low-temperature CO_2 methanation over Ni catalysts supported on nanocrystalline CeO_2 in an electric field

Ryota Yamano, Takuma Higo and Yasushi Sekine *

Received 10th November 2025
Accepted 16th February 2026

DOI: 10.1039/d5ra08683c

rsc.li/rsc-advances

Nickel catalysts supported on nanocrystalline CeO_2 exhibit intriguing properties, including high Ni dispersion, a high concentration of lattice oxygen defects in the support, and facile formation of hydroxyl groups on the Ni surface. In an electric field, CO_2 methanation was carried out using a Ni/CeO_2 catalyst. The reaction occurred even at around 393 K, a low temperature at which no activity was observed under conventional thermal conditions. In the CO_2 methanation environment, the amount of surface OH groups increased when an electric field was applied. Furthermore, adsorption species like hydroxy carbonyl, which were not detectable without the electric field, were identified. These findings suggest that applying an electric field influences the interface between Ni nanoparticles and CeO_2 particles, promoting the formation of oxygen vacancies and OH species on the Ni/CeO_2 catalyst. This enhances CO_2 activation, allowing the reaction to proceed at lower temperatures.

1 Introduction

As an effective technology for CO_2 utilisation, CO_2 methanation the Sabatier reaction:

$$CO_2 + 4H_2 \rightarrow CH_4 + 2H_2O \quad (1)$$

has attracted considerable attention.[1,2] The produced CH_4 can be utilised as fuel and can be transported easily *via* existing gas pipelines. This reaction aligns with the concept of power-to-gas.[3]

For the conventional thermo-catalytic methanation reaction, a Ni-supported or Ru-supported catalyst is typically used. The process is generally conducted at 573–673 K to achieve sufficiently high conversion of CO_2.[4] However, because CO_2 methanation is an exothermic reaction, a dilemma exists between the need for high temperatures for CO_2 activation and the thermodynamic constraints imposed by the equilibrium.[5] Therefore, operating at lower temperatures, where the equilibrium conversion can reach up to 100% and renewable energy can be used efficiently, is desirable for on-site, on-demand CH_4 production.

Many non-conventional approaches have been applied to promote the CO_2 conversion reaction, including methanation at milder conditions.[6–9] Recently, the promotion of catalytic reactions at lower temperatures has been achieved by applying a DC electric field, which imposes a weak current on a catalyst with semiconducting properties.[10,11] For various reactions (*e.g.*, NH_3 synthesis, water gas shift), relatively high catalytic activity was observed when DC electric fields were applied to semiconducting heterogeneous catalysts, even at low temperatures where the reaction rate is very low for catalysis by heating alone.[12–20] In this system, the electric field can assist the migration and activation of ionic species (*e.g.*, H^+,[21] O^{2-},[22]) on the catalyst surface and can induce new reaction pathways different from those of conventional thermo-catalytic reactions, which contribute to facile activation of stable molecules such as N_2 and CH_4. In addition, lowering the reaction temperature has been achieved successfully in several CO_2-based catalytic reactions.[23,24] Among them, the promotion of CO_2 methanation at low temperatures has been also reported,[25] however, the detailed reaction mechanism and the specific catalytic properties contributing to the activity enhancement have not yet been fully elucidated.

In reactions that apply an electric field, particularly CO_2 conversion reactions, the relationship between surface proton migration and redox processes must be considered to elucidate the reaction mechanism and identify factors that enhance catalytic activity. Factors related to surface proton migration include the amount of surface OH species[26] and the strength of OH bonds,[27] whereas those related to lattice oxygen activation include the concentration of oxygen vacancies in the metal oxide support and the ease of redox.[28] Among various metal oxides, CeO_2 is particularly suitable for reactions because of its diverse catalytic functionalities related to surface hydroxyls and the redox property, as well as its moderate semiconductivity.[29,30]

Earlier reports have described a correlation between the morphology of CeO_2 (*e.g.*, crystal structure) and its physical

Department of Applied Chemistry, Waseda University, 3-4-1, Okubo, Shinjuku, Tokyo, 169-8555, Japan. E-mail: ysekine@waseda.jp

properties, such as the amount of lattice oxygen defects[31] and surface OH groups,[32,33] suggesting the possibility of further enhancing activity in electric field-assisted catalysis using structurally controlled CeO_2-based catalysts.

To explore catalysts with high activity for CO_2 methanation in an electric field, we specifically examined Ni catalysts supported on CeO_2 with different crystalline particle sizes. The Ni catalyst supported on nanocrystalline CeO_2 with a particle size of a few nanometres exhibited high activity even at a low temperature of 373 K. Therefore, we investigated the reaction mechanism particularly focusing on the activation of surface hydroxyl groups or lattice oxygen, which is expected to be promoted under an electric field. Thereby, we examined how the structure and physical properties of CeO_2 influence these phenomena and contribute to methanation activity.

2 Experimental

2.1. Catalyst preparation and activity tests

For this study, nanocrystalline CeO_2 (NC), an aggregate of microcrystals,[34] and polycrystalline CeO_2 (PC; JRC-CEO-1), a reference catalyst supplied by the Catalysis Society of Japan, were used as supports. Nickel acetate was used as a precursor to prepare two Ni catalysts by an impregnation method. Catalysts were prepared by evaporation-drying nickel acetate onto the respective supports. Catalytic activity tests were conducted in a fixed-bed, atmospheric-pressure flow reactor, as depicted in Fig. S1. The quartz reaction tube had an inner diameter of 6 mm and an outer diameter of 8 mm. A 100 mg amount of catalyst with a particle size of 355–500 μm was placed at the centre of the reactor. Two stainless steel electrodes were inserted above and below the catalyst bed to apply the direct current (DC) electric field.

For the pre-reduction step, the catalyst was treated with a gas mixture of H_2 : Ar (1 : 3, 100 mL min^{-1}) at 773 K for 1 h. The reaction was conducted under a gas composition of CO_2 : H_2 : Ar = 1 : 4 : 5 (100 mL min^{-1}) with a GHSV of about 21 000 h^{-1}. In the case without an electric field (*i.e.*, heated catalysis), the catalytic activities were evaluated at temperatures ranging from 473 to 523 K, as at lower temperatures below 473 K, we could not observe any catalytic activity without the electric field. For tests in an electric field, the activity was evaluated at temperatures ranging from 393 to 523 K. A DC current of 5 mA was applied under these electric field conditions. The response voltage was monitored using an oscilloscope (TDS 3052B; Tektronix, Inc). Gas analysis was performed using a gas chromatograph (GC-FID, GC-14B; Shimadzu Corp.) with a Porapak-N packed column for separation. A methanizer (Ru/Al_2O_3 catalyst) was used to hydrogenate CO_2 and CO to CH_4, thereby enabling detection by the FID. The detected products included CO, CH_4, and CO_2. Based on the inlet and outlet gas compositions, CO_2 conversion, CH_4 selectivity, and carbon balance were calculated using the following equations, where F_{in} [mmol min^{-1}] and F_{out} [mmol min^{-1}] respectively represent the molar flow rates of each component at the reactor inlet and outlet. To remove water from the product gas, a moisture trap with a weak acid is used at the reactor outlet, allowing some unreacted carbon dioxide to be slightly dissolved there. The carbon dioxide consumption rate is therefore calculated from the inlet gas flow rate and the outlet product flow rate, rather than taking the difference in carbon dioxide at the inlet and outlet. The overall material balance is almost 100%. Only CO and CH_4 were detected as carbon-containing products, indicating negligible carbon deposition.

$$CO_2 \text{ conversion } (\%) = (F_{CO,out} + F_{CH_4,out}) / F_{CO_2,in} \times 100 \quad (2)$$

$$CH_4 \text{ selectivity } (\%) = F_{CH_4,out}/(F_{CO,out} + F_{CH_4,out}) \times 100 \quad (3)$$

$$\text{Carbon balance}(\%) = \frac{\text{Carbon moles of output compounds}(CO,\ CH_4,\ \text{and}\ CO_2)}{\text{Carbon moles of input } CO_2} \quad (4)$$

2.2. Characterisation of catalysts

The specific surface area of the catalysts was determined using the Brunauer–Emmett–Teller (BET) method based on N_2 adsorption. Measurements were conducted using an automated surface area analyser (Gemini VII 2390; Micromeritics Instrument Corp). Before measurement, the catalyst samples were degassed under an N_2 atmosphere at 473 K for 2 h as a pretreatment.

Field-emission transmission electron microscopy (FE-TEM) was used to analyse the morphology of CeO_2 and the particle size distribution of Ni. Observations were made using a microscope (JEM-2100F; JEOL Ltd.) operated at an acceleration voltage of 200 kV. Elemental mapping was conducted using energy-dispersive X-ray spectroscopy (EDX). Sample preparation involved dispersing a small amount of catalyst powder in ethanol, followed by its subsequent deposition onto a copper microgrid (NP–C15; Okenshoji Co., Ltd.).

X-Ray diffraction (XRD) analysis was used to examine the crystal structure of the catalysts. The measurements were performed using a diffractometer (RINT-Ultima III; Rigaku Corp.) with Cu $K\alpha$ radiation. The instrument operated at a tube current of 40 mA, tube voltage of 40 kV, and a scanning speed of 20° min^{-1}.

X-ray photoelectron spectroscopy (XPS) was conducted to investigate the hydroxyl group content and the electronic structure of the catalyst surface. Measurements were performed using a VersaProbe II system (Ulvac-PHI, Inc.) equipped with a monochromatic Al $K\alpha$ X-ray source (1486.6 eV). For measurements of the as-prepared catalysts, a pretreatment was conducted at 773 K for 1 h under an Ar flow (100 mL min^{-1}) to remove adsorbed species, such as water vapour and CO_2, from exposure to ambient air at room temperature. For evaluation of the catalyst treated under an applied electric field, after the catalyst was first pretreated at 773 K for 1 h under an Ar flow (100 mL min^{-1}), a DC current of 5 mA was applied in a H_2 : Ar gas mixture (1 : 1, 100 mL min^{-1}) at 423 K for 1 h. After pretreatment, the samples were handled in a glovebox to prevent air exposure. They were transferred to the XPS chamber using a sealed transfer vessel. The resulting spectra were

charge-corrected using the C 1s peak at 284.8 eV. The background was subtracted using the Proctor-Sherwood-Shirley method.[35,36] Peak fitting was performed using a pseudo-Voigt function (a sum of Gaussian and Lorentzian components).

In situ X-ray absorption fine structure (XAFS) measurements at the Ce L_3-edge, including X-ray absorption near-edge structure (XANES), were performed at beamline BL14B2 of SPring-8 to investigate changes in the electronic state of Ce in the catalyst under a reducing atmosphere. Sample discs (10 mm diameter) were prepared by mixing each catalyst powder with an appropriate amount of BN. As reference materials for Ce^{3+} and Ce^{4+}, we used CeF_3 and CeO_2, respectively. For measurements, the temperature was ramped from room temperature to 773 K at a rate of 10 K min^{-1} under a $H_2:N_2$ gas mixture (1 : 9, total flow rate 100 mL min^{-1}). Spectra were recorded at every 100 K interval starting from 373 K. Data processing was conducted using xTunes software (Science and Technology Research Institute Co., Ltd.).

Diffuse reflectance infrared Fourier transform spectroscopy (*in situ* DRIFTS) was used to investigate the surface-adsorbed species under reaction conditions. A schematic image of the apparatus used for measurements is presented in Fig. S2. Measurements were conducted using a spectrometer (FT/IR-6200; Jasco Corp.) equipped with a liquid nitrogen-cooled MCT detector and a ZnSe window. The DRIFTS cell, designed for electric field application, was made of Teflon, with two platinum wires inserted through the pores to serve as electrodes. The sample consisted of approximately 100–120 mg of a well-polished Ni/CeO_2 catalyst. First, the catalyst was pretreated under a reducing atmosphere ($H_2:Ar$ = 1 : 1, 40 mL min^{-1}) at 773 K (without EF) or 573 K (with EF) for 1 h with subsequent purging with Ar (40 mL min^{-1}) for 1 h. Then the catalyst was treated again with $H_2:Ar$ (40 mL min^{-1}) at 773 K (without EF) or 573 K (with EF) for an additional hour. Background spectra were collected under Ar flow (40 mL min^{-1}) at 373 K (with EF) or 473 K (without EF), after which the measurement began under reaction conditions. To observe changes in surface species before and after EF application, the reaction gas was set as $CO_2:H_2:Ar = 1:4:5$ (40 mL min^{-1}). To investigate the surface protonics effect induced by the electric field, a mixture of $H_2:Ar = 4:5$ (36 mL min^{-1}) was used. After recording changes before and after EF application, 4 mL min^{-1} of CO_2 was introduced. A direct current of 5 mA was applied during electric field operation. All spectra were collected with a resolution of 4 cm^{-1} and were averaged over 100 scans.

3 Results and discussion

3.1. Structure and morphology of catalysts

The ICP-OES analyses revealed that the Ni loading is 4.8 wt% for the Ni/CeO_2(NC) catalyst and 4.7 wt% for the Ni/CeO_2(PC) catalyst. The BET surface area of the Ni/CeO_2 (NC) catalyst and that of the Ni/CeO_2 (PC) catalyst were almost identical (152 m^2 g^{-1} and 157 m^2 g^{-1}, respectively). Therefore, the effect of surface area can be ruled out. The crystalline structures of the catalysts, primarily CeO_2, were further compared using XRD analysis, with the results presented in Fig. S3 and Table S1. No peak corresponding to metallic Ni or NiO was detected in either catalyst. Both samples exhibited diffraction patterns characteristic of a face-centred cubic fluorite structure, indicating no significant structural differences in CeO_2. However, a comparison of the diffraction peaks corresponding to each crystal plane revealed that the Ni/CeO_2 (PC) catalyst exhibited a decrease in peak intensity, suggesting lower crystallinity or increased structural disorder compared to Ni/CeO_2 (NC).

To compare the structural properties of Ni/CeO_2 catalysts, FE-TEM measurements were conducted. The results are presented in Fig. 1 and 2. In the STEM images of each catalyst, CeO_2 (NC) appeared as fine spherical particles with an average size of approximately 5 nm, whereas CeO_2 (PC) mainly consisted of large grains exceeding 100 nm in diameter. Regarding the state of supported Ni, STEM-EDS mapping revealed that Ni atoms were highly dispersed showing particle sizes within 5 nm due to suppressed aggregation (Fig. 1). In contrast, in the Ni/CeO_2 (PC) catalyst, Ni atoms were observed to aggregate into particles larger than 20 nm (Fig. 2).

3.2. Evaluation of chemical properties of catalysts

Because lattice oxygen defects on the substrate surface are known to contribute to the activity of both conventional methanation reactions and certain electric field-catalysed reactions.[37] We investigated the presence of the lattice oxygen defects in Ni/CeO_2 catalysts using Raman spectroscopy. The Raman spectra for each catalyst are depicted in Fig. 3. Among the peaks commonly observed for both catalysts, the bands around 460 cm^{-1} and 590 cm^{-1} are attributed, respectively, to the F_{2g} and D vibrational modes of the fluorite-type structure.[38,39]

The intensity ratio of these peaks (I_D/I_{F2g}) correlates with the amount of lattice oxygen defects in CeO_2. This ratio, calculated for each catalyst, revealed that the Ni/CeO_2 (NC) catalyst (I_D/I_{F2g} = 0.37) contains more lattice oxygen defects than the Ni/CeO_2 (PC) catalyst (I_D/I_{F2g} = 0.24). This result supports earlier findings indicating that lattice oxygen defects are formed more readily as the CeO_2 particle size decreases.[40] Reportedly, nanoscale CeO_2 particles exhibit more significant lattice distortion,[41] *i.e.*, changes in Ce–O bond length, accompanying defect formation. Additionally, other studies[42] have indicated that, as CeO_2 particle size decreases, crystal facets with higher Miller indices and under-coordinated sites that favour defect formation become more prevalent. This observation is consistent with our XRD results, which confirmed that CeO_2 (NC) exhibits a higher proportion of high-index planes compared to CeO_2 (PC).

Fig. S4 summarises the H_2-TPR and CO_2-TPD results for each catalyst. The H_2-TPR profile (a) shows two major features: the peak at around 473 K (α) is assigned to the reduction of NiO species weakly interacting with the CeO_2 support (*i.e.*, relatively large NiO particles), whereas the peak at around 523 K (β) is attributed to NiO strongly interacting with CeO_2 (*i.e.*, comparatively smaller NiO particles) and/or interfacial Ni–O–Ce species.[43] Comparing these two catalysts, the β peak is pronounced for Ni/CeO_2 (NC) but is barely discernible for Ni/

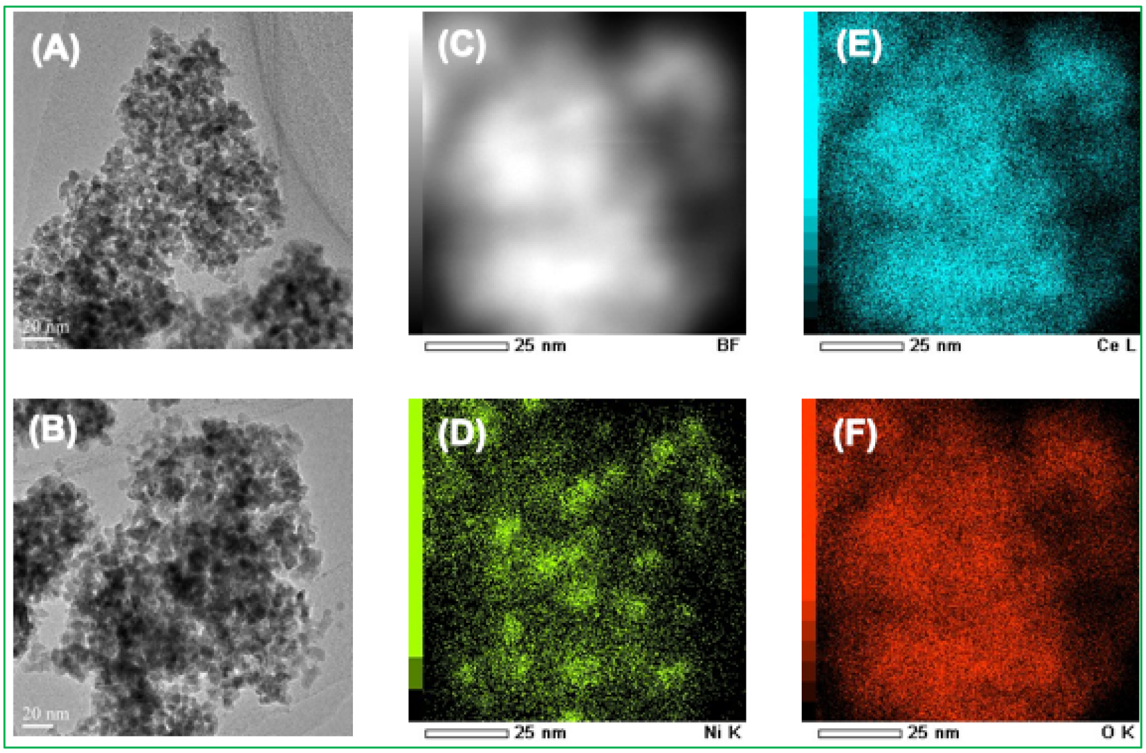

Fig. 1 (A and B) TEM, (C) HAADF-STEM images, and (D–F) corresponding EDX elemental maps of the Ni/CeO_2 (NC) catalyst.

CeO_2 (PC). This trend is consistent with FE-TEM observations, which indicate higher Ni dispersion on Ni/CeO_2 (NC), and with Raman spectra suggesting more readily reducible Ni–CeO_2 interfaces and a greater propensity for lattice oxygen vacancy formation. In the CO_2-TPD measurements, a peak appears at around 390 K, assigned to the desorption of bicarbonate

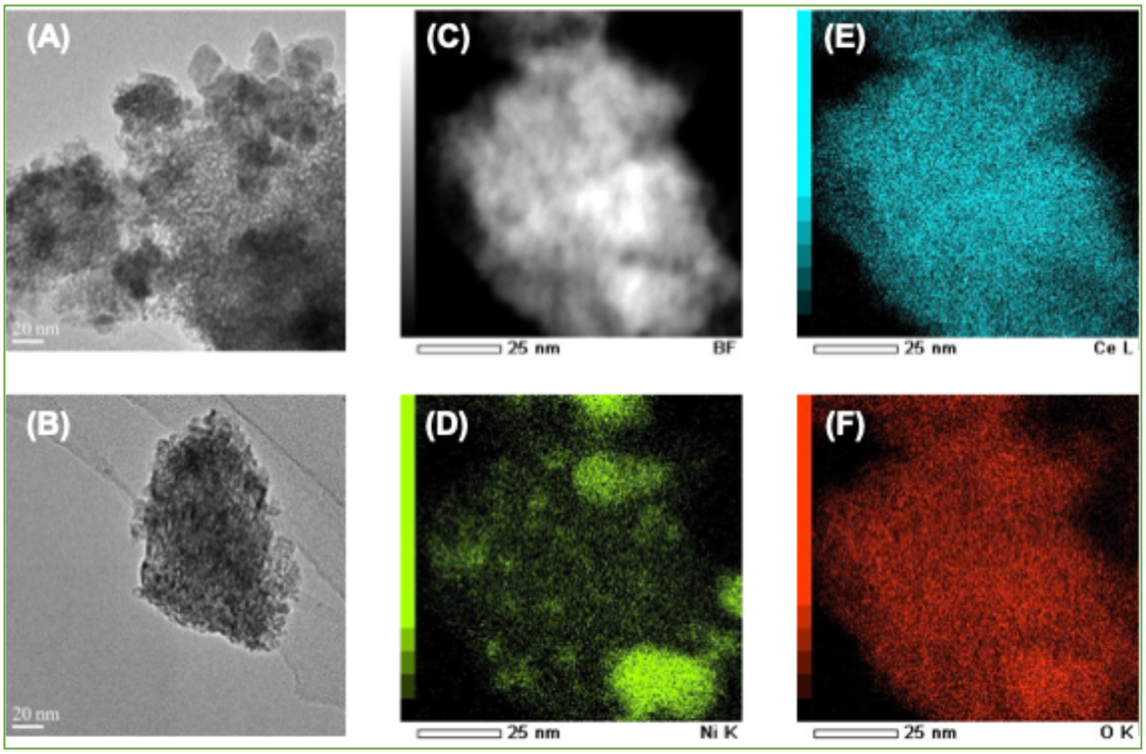

Fig. 2 (A and B) TEM, (C) HAADF-STEM images, and (D–F) corresponding EDX elemental maps of the Ni/CeO_2 (PC) catalyst.

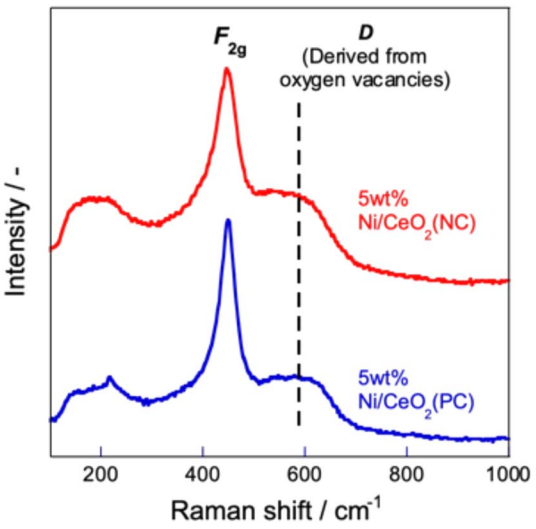

Fig. 3 Raman spectra of the Ni/CeO_2 (NC or PC) catalysts.

adsorbed on weak basic sites.[44] Comparison of peak areas (as a proxy for adsorption amount) indicates higher CO_2 uptake for Ni/CeO_2 (NC), which is likely attributable to its higher concentration of lattice oxygen vacancies.

Subsequently, XPS measurements were taken of the as-prepared catalysts to elucidate the surface hydroxyl group content and the electronic structure of the catalysts. As shown in Fig. S5 and S6, the Ce 3d spectrum exhibits four Ce^{3+} and six Ce^{4+} peaks.[45] The Ni $2p_{3/2}$ spectrum displays three characteristic peaks: NiO (854 eV), $Ni(OH)_2$ (855.5 eV), and a satellite peak (861 eV).[46,47] The O 1s spectrum shows two major components: a peak around 529 eV attributed to Ce^{4+}–O bonds in CeO_2, and another around 531.5 eV associated with Ce^{3+}–O bonds, which are attributed mainly to surface adsorbates, particularly hydroxyl groups formed on the CeO_2 surface.[48] The composition ratios of each peak, determined through spectral fitting, are presented in Table 1. Specific examination of the Ni $2p_{3/2}$ and O 1s peaks reveals that the Ni/CeO_2 (NC) catalyst contains a greater amount of hydroxyl groups on the Ni surface in the as-prepared state, whereas the Ni/CeO_2 (PC) catalyst shows a higher concentration of hydroxyl groups on the CeO_2 surface. Over the Ni/CeO_2 (NC) catalyst with Ni smaller particles, as observed *via* FE-TEM measurements, Ni–OH bonds tend to be more stable due to the rise of the d-band centre level.[49,50] In addition, lattice oxygen defects, which generally tend to form more readily at the metal-support interface due to the effect of metal-support interactions, promote the dissociation of H_2O and H_2 and contribute to OH group formation.[51] Based on these factors, it is considered that the Ni/CeO_2 (NC) catalyst readily forms OH groups near the Ni–CeO_2 interface.

Table 1 Fitting results from Ce 3d, Ni $2p_{3/2}$, and O 1s XPS spectra for as-made Ni/CeO_2 (NC) catalyst and the as-made Ni/CeO_2 (PC) catalyst

	Ratio%					
	Ce 3d		Ni $2p_{3/2}$		O 1s	
Catalyst	Ce^{3+}	Ce^{4+}	NiO	$Ni(OH)_2$	Ce–O_{lnt}	Ce–OH
5 wt% Ni/CeO_2 (NC)	29.8	70.2	38.9	61.1	66.3	33.7
5 wt% Ni/CeO_2 (PC)	31.9	68.1	50.8	49.2	45.6	54.4

To investigate the reduction behaviour of Ce, *in situ* XAFS measurements at the Ce L_3-edge were conducted under a hydrogen atmosphere. The results are presented in Fig. 4. For both catalysts, a shift in the absorption edge from the high-valence state (Ce^{4+}) to the low-valence state (Ce^{3+}) was observed as the temperature increased. It is noteworthy that Ni/CeO_2 (PC) exhibited a larger shift toward the lower valence state than Ni/CeO_2 (NC), indicating that Ce in Ni/CeO_2 (PC) is more readily reduced to Ce^{3+} under hydrogen, which is consistent with XPS results. In general, when CeO_2 interacts with H_2, two types of dissociation can occur: homogeneous dissociation, resulting in the formation of surface hydroxyl (OH) groups, and heterogeneous dissociation, producing hydride (H^-) and OH species. In CeO_2 with a high concentration of lattice oxygen, the Ce–H species, where H^- is bound to a Ce atom, has been reported as stable.[47,48,52] Therefore, it is suggested that in CeO_2 (PC), homogeneous dissociation of H_2 is predominant, leading primarily to the formation of surface OH groups. By contrast, CeO_2 (NC) tends to favour heterogeneous dissociation under reducing conditions, resulting in the formation of hydride species.

3.3. Methanation activity over the Ni/CeO_2 catalyst in an electric field

The catalytic activities of CO_2 methanation over the Ni/CeO_2 (NC or PC) catalysts were evaluated at temperatures of 393 to 523 K (Fig. 5). When comparing the two catalysts, even under heating without an electric field, the Ni/CeO_2 (NC) catalyst exhibited a higher CO_2 conversion rate than the Ni/CeO_2 (PC) catalyst (blue-filled circles and blue circles in Fig. 5). Next, activity tests were conducted with an electric field applied (red plots). It is particularly interesting that both catalysts exhibited methanation activity even at 393 K, with NC showing higher activity. However, when the electric field was turned off, no activity was observed at these low temperatures, suggesting that the electric field influences adsorbed species on the catalyst surface. In these experiments, it has already been established through numerous previous investigations that the effect of Joule heating induced by the applied electric field on catalytic activity is negligible[16,19] and no significant changes in the catalyst structure, such as the agglomeration of Ni particles, were observed after the reaction in an applied electric field (Fig. S7). For the NC catalyst, even at 393 K, it exhibited very high methane selectivity exceeding 95% in the presence of an electric field. In contrast, the PC catalyst showed methane selectivity of approximately 60% at 393 K.

3.4. Adsorbed species in reaction atmosphere in an electric field

To identify surface-adsorbed species and reaction intermediates of CO_2 methanation on Ni/CeO_2 catalysts, *in situ* DRIFTS

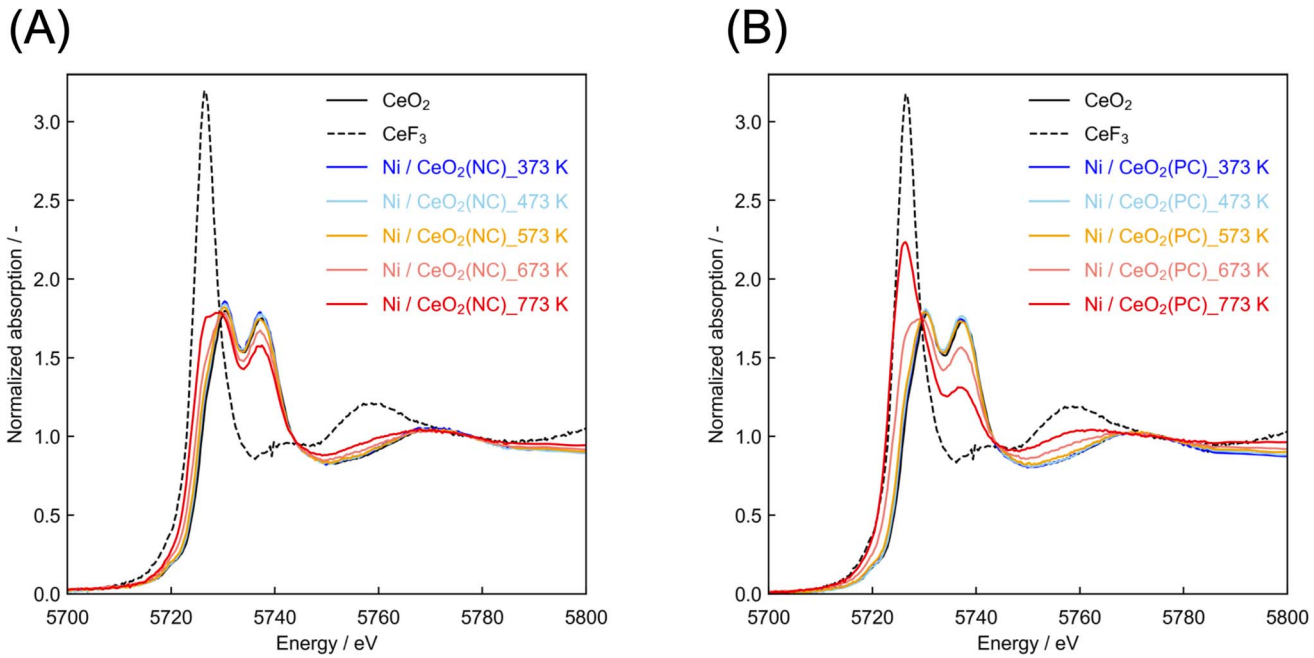

Fig. 4 XAFS spectra under the *in situ* condition of each temperature (A) over Ni/CeO_2 (NC) and (B) over Ni/CeO_2 (PC).

measurements were conducted. First, the *in situ* DRIFT spectra of the Ni/CeO_2 (NC) catalyst without an applied electric field are depicted in Fig. 6. The results reveal the adsorption of bicarbonate (1008 cm^{-1}, 1246 cm^{-1}, 1422 cm^{-1}), monodentate carbonate (1092 cm^{-1}, 1485 cm^{-1}), bidentate carbonate (1051 cm^{-1}, 1285 cm^{-1}, 1557 cm^{-1}), bridged formate (1398 cm^{-1}, 1598 cm^{-1}, 2841 cm^{-1}, 2950 cm^{-1}), CO species adsorbed onto the Ni surface (1917 cm^{-1}, 2027 cm^{-1}), and gas-phase CH_4 (3012 cm^{-1}).[53–55] As the temperature increased from 473 to 523 K, the formate-related peak intensity decreased, whereas the CH_4 signal increased, suggesting the consumption of formate species as an intermediate in CH_4 formation. *In situ* DRIFTS measurements were also conducted for the Ni/CeO_2 (PC) catalyst under the same conditions as those used for the Ni/CeO_2 (NC) catalyst without the application of an electric field (Fig. S8). In contrast to the Ni/CeO_2 (NC) catalyst, no CO adsorption on the Ni surface was observed. Moreover, the peak intensities corresponding to bicarbonate, carbonate, and formate species were weaker than those observed for the Ni/CeO_2 (NC) catalyst.

Next, *in situ* DRIFTS measurements were performed on the Ni/CeO_2 (NC) catalyst under an applied current of 5 mA to

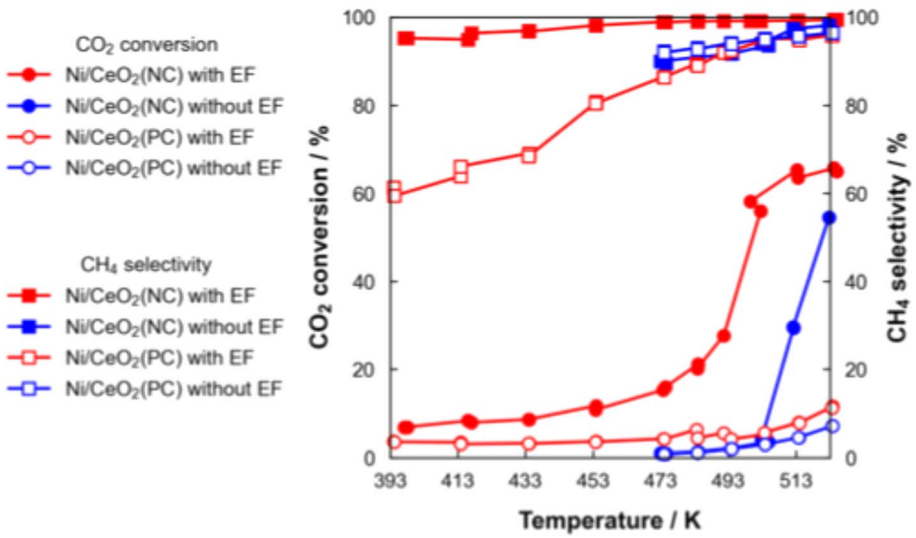

Fig. 5 CO_2 conversion and CH_4 selectivity for activity tests over the Ni/CeO_2 (NC or PC) catalysts with or without the electric field at various temperatures ($CO_2 : H_2 : Ar = 1 : 4 : 5$; 100 mL min^{-1} total flow rate; 100 mg catalyst weight).

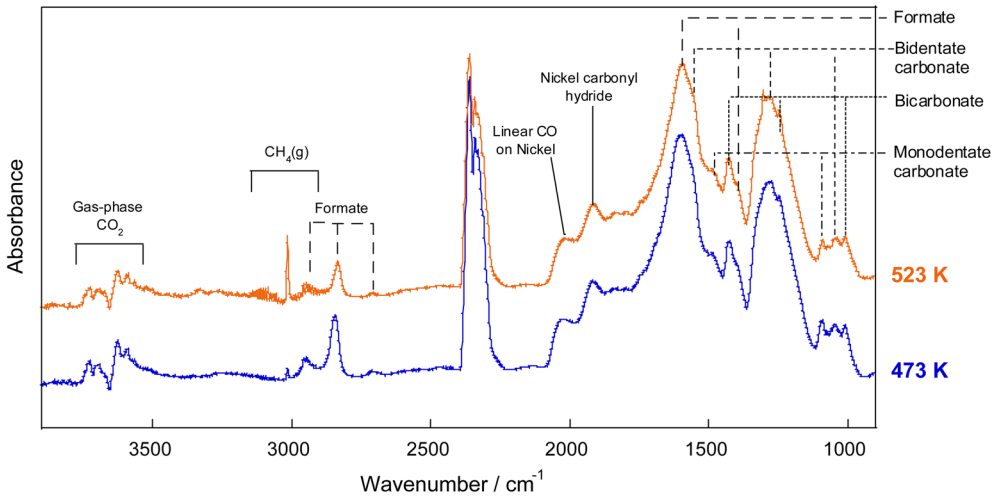

Fig. 6 *In situ* DRIFT spectra under the reaction atmosphere over the Ni/CeO_2 (NC) catalyst without an electric field at 473–523 K ($CO_2 : H_2 : Ar = 1 : 4 : 5$; 40 mL min^{-1} total flow rate).

investigate the reaction mechanism under an electric field. As depicted in Fig. 7, adsorbed species, including hydroxy carbonyl (1335 cm^{-1}) and bridged carbonate (1132 cm^{-1}), were observed.[56,57] When an electric field was applied under H_2-only flow (Fig. 8), peaks corresponding to Ce–OH species were observed, specifically, Ce^{3+}–OH at 3650 cm^{-1} and Ce^{4+}–OH at 3674 cm^{-1}.[58,59] These results suggest that the electric field promotes the formation of surface hydroxyl groups necessary for surface proton conduction. When CO_2 gas was introduced under these conditions, hydroxycarbonyl species were observed, similar to those detected under direct electric-field application during simultaneous CO_2 and H_2 supply. However, the Ce^{3+}–OH and gas-phase CO peak intensities were higher than those presented in Fig. 7.

In situ DRIFTS measurements were also conducted for the Ni/CeO_2 (PC) catalyst under the same electric field conditions as those used for the Ni/CeO_2 (NC) catalyst (Fig. S9 and S10). As in the Ni/CeO_2 (NC) system, peaks corresponding to hydroxy carbonyl, bridged carbonate, Ce^{3+}–OH, and Ce^{4+}–OH were observed. However, the intensities of all these peaks were lower than those found for the Ni/CeO_2 (NC) catalyst.

To verify the formation of OH species on the catalyst surface by applying an electric field, we performed XPS measurements using Ni/CeO_2 (NC) before and after H_2 treatment, with the electric field applied. The XPS spectra are shown respectively in Fig. S11 and S12. The composition ratios of each peak, as determined by spectral fitting, are presented in Table 2. After application of the electric field, the amounts of hydroxyl groups on both the Ni surface and the CeO_2 surface increased for the

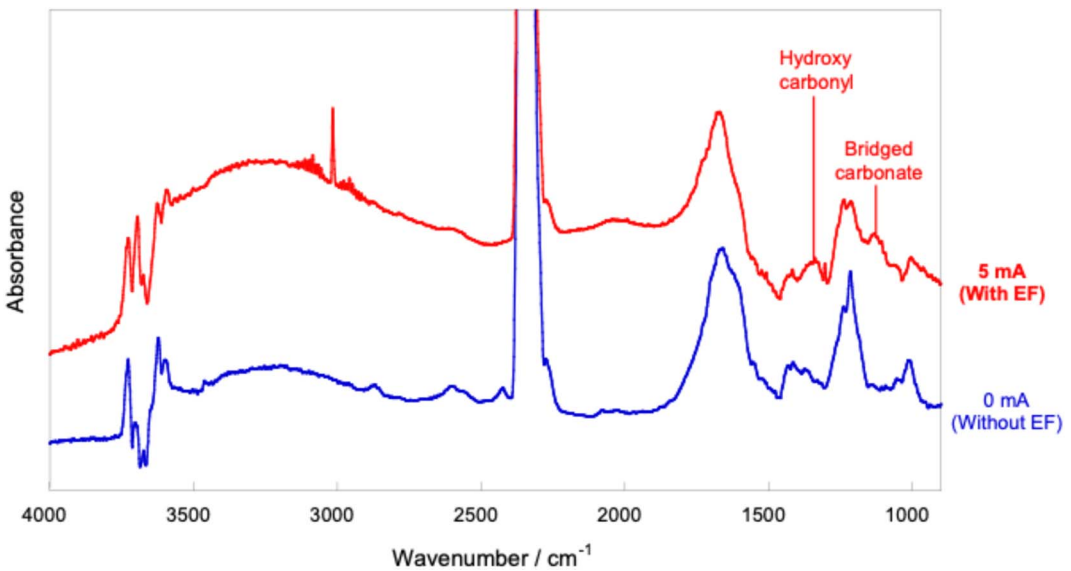

Fig. 7 *In situ* DRIFT spectra under the reaction atmosphere over the Ni/CeO_2 (NC) catalyst recorded before/during application of the electric field (EF) at 423 K, $CO_2 : H_2 : Ar = 1 : 4 : 5$; 40 mL min^{-1} total flow rate, 0 or 5.0 mA imposed current.

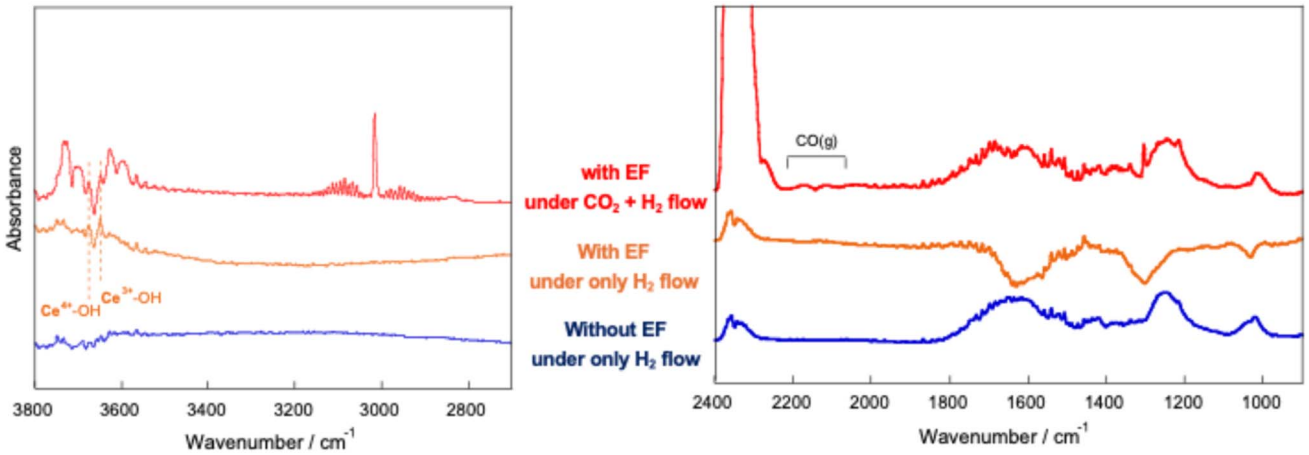

Fig. 8 *In situ* DRIFT spectra under only H_2 flow over the Ni/CeO_2 (NC) catalyst recorded before/during application of the electric field (EF) at 423 K, H_2 : Ar = 1 : 1; 40 mL min^{-1} total flow rate, 0 or 5.0 mA imposed current.

Table 2 Fitting results from Ce 3d, Ni $2p_{3/2}$ and O 1s XPS spectra for the Ni/CeO_2 (NC) catalyst before applying EF and the Ni/CeO_2 (NC) catalyst after applying EF

	Ratio%					
	Ce 3d		Ni $2p_{3/2}$		O 1s	
Catalyst	Ce^{3+}	Ce^{4+}	NiO	$Ni(OH)_2$	Ce–O_{lnt}	Ce–OH
Before applying EF	29.8	70.2	38.9	61.1	66.3	33.7
After applying EF	33.9	66.1	16.9	83.1	55.0	45.0

Ni/CeO_2 (NC) catalyst. Results showed that applying the electric field can promote OH formation on the catalyst surface.

3.5. Elucidation of the reaction mechanism

In earlier reports, two mechanisms for thermal CO_2 methanation in the absence of an electric field were proposed: an associative mechanism[60] proceeding *via* formate species on the support, and a dissociative mechanism[61,62] proceeding *via* CO intermediates on the active metal surface. Fig. 9 presents the presumed mechanism for CO_2 methanation in the absence of an electric field over the Ni/CeO_2 catalyst. In this study, *in situ* DRIFTS measurements revealed the simultaneous formation of formate species and adsorbed CO on Ni/CeO_2 (NC). According to reports, the dissociative mechanism tends to occur at the metal-support interface in catalysts with lattice-oxygen defects.[62] These results suggest that both associative and dissociative pathways occur in parallel under these conditions. In contrast, for the Ni/CeO_2 (PC) catalyst, no peak corresponding to adsorbed CO was observed, suggesting that only the associative mechanism is active in this system.

Regarding the reaction mechanism under electric field application, earlier studies have demonstrated that an external electric field can influence the adsorption and reactivity of surface species, including hydroxyls, through DFT calculation,[63–65] and that imposing the electric field on Ni catalysts can engender the formation of $Ni(OH)_2$ as well as hydroxyls on the CeO_2 surface. A coupled site of a lattice oxygen vacancy and an adjacent hydroxyl group can act as a Lewis base, promoting CO_2 adsorption and activation.[65,66] It is therefore assumed that bridged carbonate species can form at the interface between the Ni surface and the oxide support *via* OH groups adsorbed onto both Ni and CeO_2 surfaces. TEM measurements reveal that the Ni/CeO_2 (NC) catalyst exhibits higher Ni dispersion compared to the Ni/CeO_2 (PC) catalyst. Generally, smaller particle sizes result in a larger overall Ni interfacial length for the catalyst. Therefore, assuming bridged carbonates form at the Ni–CeO_2 interface, the Ni/CeO_2 (NC)

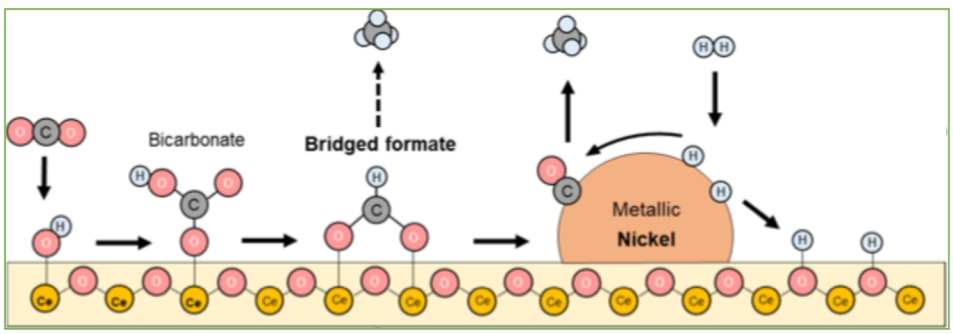

Fig. 9 Schematic illustration of the proposed mechanism in the CO_2 methanation reaction without the electric field over the Ni/CeO_2 catalyst.

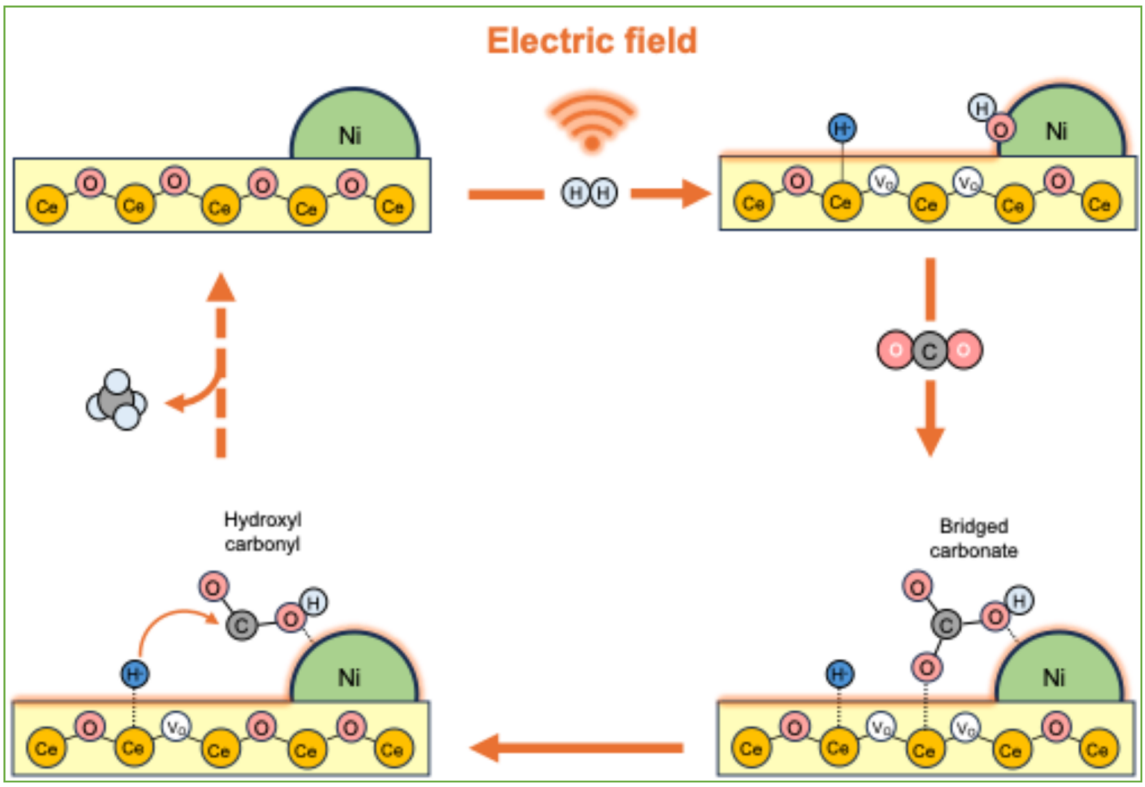

Fig. 10 Schematic illustration of the proposed mechanism of the CO_2 methanation reaction with the electric field over the Ni/CeO_2 catalyst.

catalyst is thought to possess more sites necessary for bridged carbonate formation than the Ni/CeO_2 (PC) catalyst. It was reported that on distorted interfacial sites (*e.g.*, interfaces between different metals or between a metal and its support, as proposed in this study), bridged species can avoid excessive stability and thus show reactivity.[67] On the other hand, hydroxy carbonyl is reported to be a reactive species generated through the utilisation of lattice oxygen defects.[68,69] In our previous study, we experimentally observed H_2 consumption and the formation of oxygen vacancies, accompanied by H_2O formation, when an electric field was applied in a hydrogen atmosphere at lower temperatures.[24,37] So, hydroxy carbonyl species can be formed effectively in the electric field.

Earlier reports have described that a catalyst surface including nanoparticles and metal-support interface experience stronger local electric fields than the bulk when semiconductors or metal nanoparticles are exposed to external stimuli such as electric fields or light, known as the "tip effect".[70–72] Accordingly, the reaction mechanism proposed for CO_2 methanation under an electric field on a Ni–CeO_2 catalyst is presented in Fig. 10. At the Ni–CeO_2 interface, where the local electric field is concentrated, H_2 dissociation and the formation of lattice oxygen vacancies are promoted. Then, CO_2 molecules utilise the resulting hydrogen species and oxygen vacancies to form highly reactive intermediates such as bridged carbonate and hydroxy carbonyl species. Furthermore, hydride species are believed to play a key role in the hydrogenation of CO_2.[73,74] As described in *in situ* XAFS measurements, such hydrides are more readily formed on CeO_2 (NC), which is thought to facilitate conversion of CO_2 to CH_4. On the other hand, the Ni/CeO_2(PC) catalyst is considered not to benefit from the applied electric field to the same extent as the Ni/CeO_2(NC) catalyst. This is likely because structural factors, such as low Ni dispersion and a low concentration of lattice oxygen vacancies, hinder the formation of Ni–OH groups and hydrides that contribute to methanation in the electric field.

4 Conclusion

We specifically examined CeO_2-supported Ni catalysts with different crystal structures and investigated catalysts that exhibit high activity in CO_2 methanation under an electric field. We investigated the reaction mechanism by particularly addressing the activation of surface hydroxyl groups and lattice oxygen under an electric field and examined how the structure and physical properties of CeO_2 affect these phenomena and contribute to methanation activity.

First, from the perspective of catalyst structure, the BET specific surface areas of Ni/CeO_2-NC and Ni/CeO_2-PC catalysts were almost identical. STEM-EDS mapping revealed that Ni supported on CeO_2-NC was highly dispersed, whereas on CeO_2-PC it was predominantly present as larger particles with an average diameter of approximately 25 nm. Raman spectroscopy revealed that the NC catalyst contained more lattice oxygen defects than the PC catalyst. XPS analysis showed that the NC catalyst had a higher amount of hydroxyl groups on the Ni surface as prepared.

The NC catalyst exhibited a higher CO_2 conversion rate than the PC catalyst under heating conditions. Furthermore, when an electric field was applied, the NC catalyst demonstrated high selectivity to methane and showed high CO_2 conversion, even at the low temperature of 393 K. *In situ* DRIFTS observations showed that cross-linked carbonate species formed at the interface between the Ni surface and the oxide support *via* OH groups, and that the reaction proceeded effectively in an electric field utilising lattice oxygen defect. CO_2 molecules utilise the generated hydrogen species and oxygen vacancies to form reactive intermediates such as bridging carbonates and hydroxy carbonyl species. Additionally, hydrogen species play a crucially important role in the hydrogenation of CO_2. These mechanisms promote the conversion of CO_2 to CH_4 on the NC catalyst under an electric field.

Conflicts of interest

There are no conflicts to declare.

Data availability

The data supporting this article have been included in the manuscript itself and in the supplementary information (SI). Supplementary information: apparatus, XRD, XPS, TPD, TEM, HAADF-STEM, and DRIFT spectra. See DOI: https://doi.org/10.1039/d5ra08683c.

Acknowledgements

For the catalyst preparation, we deeply appreciate Dr Tasuku Komanoya for his assistance. A part of this work was supported by JSPS KAKENHI Grant Numbers 23H05404, 24H00487, and 23K20034.

References

1 J. Artz, T. Müller, K. Thenert, J. Kleinekorte, R. Meys, A. Sternberg, A. Bardow and W. Leitner, *Chem. Rev.*, 2018, **118**, 434–504.
2 C. Hepburn, E. Adlen, J. Beddington, E. A. Carter, S. Fuss, N. Mac Dowell, J. C. Minx, P. Smith and C. K. Williams, *Nature*, 2019, **575**, 87–97.
3 S. Abate, G. Centi, F. Krebs, C. Mebrahtu, R. Palkovits and S. Perathoner, *Stud. Surf. Sci. Catal.*, 2019, **178**, 85–103.
4 M. A. A. Aziz, A. A. Jalil, S. Triwahyono and A. Ahmad, *Green Chem.*, 2015, **17**, 2647–2663.
5 P. Li, B. Wen, F. Yu, M. Zhu, J. Xu and Y. Huang, *J. Energy Chem.*, 2016, **25**, 553–565.
6 R. Snoeckx and A. Bogaerts, *Chem. Soc. Rev.*, 2017, **46**, 5805–5863.
7 V. Kumaravel, J. Bartlett and S. C. Pillai, *ACS Energy Lett.*, 2020, **5**, 486–519.
8 C. Fukuhara, A. Kamiyama, M. Itoh, N. Hirata, S. Sakhon, M. Sudoh and R. Watanabe, *Chem. Eng. Sci.*, 2020, **219**, 115589.
9 C. Molinet-Chinaglia, S. Shafiq and P. Serp, *ChemCatChem*, 2024, **16**, e202401213.
10 Y. Sekine, M. Tomioka, M. Matsukata and E. Kikuchi, *Catal. Today*, 2009, **146**, 183–187.
11 F. Che, J. T. Gray, S. Ha, N. Kruse, S. L. Scott and J.-S. McEwen, *ACS Catal.*, 2018, **8**, 5153–5174.
12 R. Manabe, H. Nakatsubo, A. Gondo, K. Murakami, S. Ogo, H. Tsuneki, M. Ikeda, A. Ishikawa, H. Nakai and Y. Sekine, *Chem. Sci.*, 2017, **8**, 5434–5439.
13 Y. Sekine, K. Yamagishi, Y. Nogami, R. Manabe, K. Oshima and S. Ogo, *Catal. Lett.*, 2016, **146**, 1423–1428.
14 T. Yabe, K. Yamada, K. Murakami, K. Toko, K. Ito, T. Higo, S. Ogo and Y. Sekine, *ACS Sustain. Chem. Eng.*, 2019, **7**, 5690–5697.
15 C. Sampson, T. Masuda, T. Horiguchi, S. Ichiguchi, H. Sampei, H. Matsubara, S. Itagaki, G. Inoue and Y. Sekine, *ACS Catal.*, 2025, **15**, 12885–12896.
16 Y. Ofuchi, K. Mitarai, S. Doi, K. Saegusa, M. Hayashi, H. Sampei, T. Higo, J.-G. Seo and Y. Sekine, *Chem. Sci.*, 2024, **15**, 15125–15133.
17 R. Maeda, H. Sampei, Y. Mizutani, T. Higo, T. Tsuda, H. Akiyama, H. Tsuneki, T. Mitsudome and Y. Sekine, *Sustain. Energy Fuels*, 2024, **8**, 2087–2093.
18 A. Shigemoto, Y. Inoda, C. Ukai, T. Higo, K. Oka and Y. Sekine, *Chem. Commun.*, 2024, **60**, 1563–1566.
19 Y. Hisai, Q. Ma, T. Qureishy, T. Watanabe, T. Higo, T. Norby and Y. Sekine, *Chem. Commun.*, 2021, **57**, 5737–5749.
20 K. Murakami, Y. Tanaka, R. Sakai, Y. Hisai, S. Hayashi, Y. Mizutani, T. Higo, S. Ogo, J.-G. Seo, H. Tsuneki and Y. Sekine, *Chem. Commun.*, 2020, **56**, 3365–3368.
21 R. Manabe, S. Okada, R. Inagaki, S. Ogo and Y. Sekine, *Sci. Rep.*, 2016, **6**, 38007.
22 K. Sugiura, S. Ogo, K. Iwasaki, T. Yabe and Y. Sekine, *Sci. Rep.*, 2016, **6**, 25154.
23 T. Yabe, K. Yamada, K. Murakami, K. Toko, K. Ito, T. Higo, S. Ogo and Y. Sekine, *ACS Sustain. Chem. Eng.*, 2019, **7**, 5690–5697.
24 R. Yamano, S. Ogo, N. Nakano, T. Higo and Y. Sekine, *EES Catal.*, 2023, **1**, 125–133.
25 K. Yamada, S. Ogo, R. Yamano, T. Higo and Y. Sekine, *Chem. Lett.*, 2020, **49**, 303–306.
26 A. Takahashi, R. Inagaki, M. Torimoto, Y. Hisai, T. Matsuda, Q. Ma, J. G. Seo, T. Higo, H. Tsuneki, S. Ogo, T. Norby and Y. Sekine, *RSC Adv.*, 2020, **10**, 14487–14492.
27 K. Murakami, Y. Mizutani, H. Sampei, A. Ishikawa, Y. Tanaka, S. Hayashi, S. Doi, T. Higo, H. Tsuneki, H. Nakai and Y. Sekine, *Phys. Chem. Chem. Phys.*, 2021, **23**, 4509–4516.
28 S. Ogo, H. Nakatsubo, K. Iwasaki, A. Sato, K. Murakami, T. Yabe, A. Ishikawa, H. Nakai and Y. Sekine, *J. Phys. Chem. C*, 2018, **122**, 2089–2096.
29 Y. Zhang, S. Zhao, J. Feng, S. Song, W. Shi, D. Wang and H. Zhang, *Chem*, 2021, **7**, 2022–2059.
30 K. Chang, H. Zhang, M.-J. Cheng and Q. Lu, *ACS Catal.*, 2020, **10**, 613–631.
31 T. Sakpal and L. Lefferts, *J. Catal.*, 2018, **367**, 171–180.

32 T. V. Plakhova, A. Yu. Romanchuk, S. M. Butorin, A. D. Konyukhova, A. V. Egorov, A. A. Shiryaev, A. E. Baranchikov, P. V. Dorovatovskii, T. Huthwelker, E. Gerber, S. Bauters, M. M. Sozarukova, A. C. Scheinost, V. K. Ivanov, S. N. Kalmykov and K. O. Kvashnina, *Nanoscale*, 2019, **11**, 18142–18149.
33 M. K. Ghosalya, X. Li, A. Beck, J. A. van Bokhoven and L. Artiglia, *J. Phys. Chem. C*, 2021, **125**, 9303–9309.
34 R. Maeda, H. Sampei, R. Nakayama, T. Higo, Y. Koshizuka, Y. Bando, T. Komanoya, Y. Nakahara and Y. Sekine, *RSC Adv.*, 2024, **14**, 9869–9877.
35 A. Proctor and P. M. A. Sherwood, *Anal. Chem.*, 1982, **54**, 13–19.
36 D. A. Shirley, *Phys. Rev. B*, 1972, **5**, 4709–4714.
37 N. Nakano, M. Torimoto, H. Sampei, R. Yamashita, R. Yamano, K. Saegusa, A. Motomura, K. Nagakawa, H. Tsuneki, S. Ogo and Y. Sekine, *RSC Adv.*, 2022, **12**, 9036–9043.
38 F. Wang, C. Li, X. Zhang, M. Wei, D. G. Evans and X. Duan, *J. Catal.*, 2015, **329**, 177–186.
39 X. Du, D. Zhang, L. Shi, R. Gao and J. Zhang, *J. Phys. Chem. C*, 2012, **116**, 10009–10016.
40 L. J. Wu, H. J. Wiesmann, A. R. Moodenbaugh, R. F. Klie, Y. M. Zhu, D. O. Welch and M. Suenaga, *Phys. Rev. B:Condens. Matter Mater. Phys.*, 2004, **69**, 125415.
41 X. Hao, A. Yoko, C. Chen, K. Inoue, M. Saito, G. Seong, S. Takami, T. Adschiri and Y. Ikuhara, *Small*, 2018, **14**, 1802915.
42 J. Xu, J. Harmer, G. Li, T. Chapman, P. Collier, S. Longworth and S. C. Tsang, *Chem. Commun.*, 2010, **46**, 1887–1889.
43 Y. Ma, J. Liu, M. Chu, J. Yue, Y. Cui and G. Xu, *Catal. Lett.*, 2022, **152**, 872–882.
44 X. Li, X. Liu, J. Hao, L. Li, Y. Gao, Y. Gu, Z. Cao and J. Liu, *ACS Omega*, 2022, **7**, 24646–24655.
45 L. Artiglia, F. Orlando, K. Roy, R. Kopelent, O. Safonova, M. Nachtegaal, T. Huthwelker and J. A. van Bokhoven, *J. Phys. Chem. Lett.*, 2017, **8**, 102–108.
46 K. Nagakawa, H. Sampei, A. Takahashi, J. Sasaki, T. Higo, N. Mori, H. Sato and Y. Sekine, *RSC Adv.*, 2022, **12**, 25565–25569.
47 C. Lv, X. Wang, L. Gao, A. Wang, S. Wang, R. Wang, X. Ning, Y. Li, D. W. Boukhvalov, Z. Huang and C. Zhang, *ACS Catal.*, 2020, **10**, 13323–13333.
48 Z. Wu, Y. Cheng, F. Tao, L. Daemen, G. S. Foo, L. Nguyen, X. Zhang, A. Beste and A. J. Ramirez-Cuesta, *J. Am. Chem. Soc.*, 2017, **139**, 9721–9727.
49 R. C. Catapan, A. A. M. Oliveira, Y. Chen and D. G. Vlachos, *J. Phys. Chem. C*, 2012, **116**, 20281–20291.
50 T. Van Haasterecht, M. Swart, K. P. De Jong and J. H. Bitter, *J. Energy Chem.*, 2016, **25**, 289–296.
51 N. Paudyal, E. W. Peterson, Y. Zhou, S. D. Senanayake and J. Zhou, *J. Phys. Chem. C*, 2025, **129**, 13723–13731.
52 Z. Li, K. Werner, L. Chen, A. Jia, K. Qian, J.-Q. Zhong, R. You, L. Wu, L. Zhang, H. Pan, X.-P. Wu, X.-Q. Gong, S. Shaikhutdinov, W. Huang and H.-J. Freund, *Chem.–Eur. J.*, 2021, **27**, 5268–5276.
53 E. T. Saw, U. Oemar, M. L. Ang, H. Kus and S. Kawi, *Catal. Sci. Technol.*, 2016, **6**, 5336–5349.
54 J. Vecchietti, G. D. Belletti, P. Quaino, A. Bonivardi and S. Collins, *ChemCatChem*, 2023, **15**, e202300435.
55 H.-X. Liu, S.-Q. Li, W.-W. Wang, W.-Z. Yu, W.-J. Zhang, C. Ma and C.-J. Jia, *Nat. Commun.*, 2022, **13**, 867.
56 Y. Guo, S. Mei, K. Yuan, D.-J. Wang, H.-C. Liu, C.-H. Yan and Y.-W. Zhang, *ACS Catal.*, 2018, **8**, 6203–6215.
57 S. M. Lee, Y. H. Lee, D. H. Moon, J. Y. Ahn, D. D. Nguyen, S. W. Chang and S. S. Kim, *Ind. Eng. Chem. Res.*, 2019, **58**, 8656–8662.
58 O. Pozdnyakova, D. Teschner, A. Wootsch, J. Kröhnert, B. Steinhauer, H. Sauer, L. Tóth, F. Jentoft, A. Knop-Gericke and Z. Paal, *J. Catal.*, 2006, **237**, 1–16.
59 A. Badri, C. Binet, A. Jadi, J. Lamotte and J.-C. Lavalley, *J. Chem. Soc., Faraday Trans.*, 1996, **92**, 4669–4673.
60 Z. Hao, J. Shen, S. Lin, X. Han, X. Y. Chang, J. Liu, M. Li and X. Ma, *Appl. Catal. B*, 2021, **286**, 119922.
61 C. Heine, B. A. J. Lechner, H. Bluhm and M. Salmeron, *J. Am. Chem. Soc.*, 2016, **138**, 13246–13252.
62 A. Cárdenas-Arenas, A. Quindimil, A. Davó-Quiñonero, E. Bailón-García, D. Lozano-Castelló, U. De-La-Torre, B. Pereda-Ayo, J. A. González-Marcos, J. R. González-Velasco and A. Bueno-López, *Appl. Catal. B*, 2020, **265**, 118538.
63 Y. Xie, J. Chen, X. Wu, J. Wen, R. Zhao, Z. Zhang, P. Gao, L. Li, C. Chang and Y. Qu, *ACS Catal.*, 2022, **12**, 10587–10602.
64 G. S. Karlberg, J. Rossmeisl and J. K. Nørskov, *Phys. Chem. Chem. Phys.*, 2007, **9**, 5158–5161.
65 S. R. Kelly, C. Kirk, K. Chan and J. K. Nørskov, *J. Phys. Chem. C*, 2020, **124**, 14581–14591.
66 H. Li, J. Zhao, L. Luo, J. Du and J. Zeng, *Acc. Chem. Res.*, 2021, **54**, 1454–1464.
67 C. Song, J. Liu, R. Wang, X. Tang, K. Wang, Z. Gao, M. Peng, H. Li, S. Yao, F. Yang, H. Lu, Z. Liao, X.-D. Wen, D. Ma, X. Li and L. Lin, *Nat. Chem. Eng.*, 2024, **1**, 638–649.
68 L. F. Bobadilla, J. L. Santos, S. Ivanova, J. A. Odriozola and A. Urakawa, *ACS Catal.*, 2018, **8**(8), 7455–7467.
69 J. A. Rodríguez, J. Evans, J. Graciani, J.-B. Park, P. Liu, J. Hrbek and J. F. Sanz, *J. Phys. Chem. C*, 2009, **113**, 7364–7370.
70 Y. Adachi, J. Brndiar, M. Konôpka, R. Turanský, Q. Zhu, H. F. Wen, Y. Sugawara, L. Kantorovich, I. Štich and Y. J. Li, *Sci. Adv.*, 2023, **9**, eadi4799.
71 Y.-C. Ruan, Y.-M. Xie, X.-L. Chen, L. Dong, F.-F. Zhang, T.-T. Yang, X.-F. Luo, M.-Y. Cheng, P.-F. Yin, C.-K. Dong, K. Lin, D.-J. Li, H. Liu and X.-W. Du, *Nano Lett.*, 2022, **22**, 9694–9703.
72 P. V. Sarma, B. V. Kramar, L. Chen, S. Sasmal, N. P. Weingartz, J. Huang, J. B. Mitchell, M. Kwak, L. X. Chen and S. W. Boettcher, *Chem. Mater.*, 2024, **36**, 11863–11872.
73 H. Shen, Y. Dong, S. Yang, Y. He, Q. Wang, Y. Cao, W. Wang, T. Wang, Q. Zhang and H. Zhang, *Nano Res.*, 2022, **15**, 5831–5841.
74 Y. Tang, Y. Kobayashi, C. Tassel, T. Yamamoto and H. Kageyama, *Adv. Energy Mater.*, 2018, **8**, 1800800.